Environmental Earth Sciences (2019) 78:267
https://doi.org/10.1007/s12665-019-8269-1

ORIGINAL ARTICLE

A comparison of numerical and Lu modeling of water flow and heat transport with laboratory experiments

Jie Ren[1,2] · Wenbing Zhang[1] · Jie Yang[1] · Zhenzhong Shen[2] · Jian Zhao[2] · Yinjun Zhou[3] · Zhenhua Wang[4]

Received: 15 February 2018 / Accepted: 12 April 2019

Abstract

Reservoirs are considered to result in significant changes to river water temperature. Discharge of deep water has a large impact on aquatic ecosystems downstream of dam and on both river banks. A laboratory sand tank test investigation was conducted to simulate water flow and thermal dynamics in the riparian zone. The sand temperature (ST) data generated were used to validate and compare HYDRUS-2D, a physically based numerical model, with Lu et al.'s (Soil Sci Soc Am J 71(1):8–14, 2007) soil thermal conductivity model under different water temperature, hydraulic head and radiation temperature conditions. The Richards model and the heat conduction model were coupled through the Horton thermal conductivity model and the Lu et al. (Soil Sci Soc Am J 71(1):8–14, 2007) model, respectively. The results demonstrated the success of model coupling and its application for investigating water flow and thermal dynamics in the riparian zone. The Lu et al. (Soil Sci Soc Am J 71(1):8–14, 2007) model based on COMSOL and the Horton thermal conductivity model based on HYDRUS each had their own advantages. Global analysis showed that the Lu et al. (Soil Sci Soc Am J 71(1):8–14, 2007) model was better able to simulate the riparian zone temperature field under the investigated experimental conditions. The sensitivity analysis results showed that the parameters n_v, T and H had a considerable influence on the temperature field in the model, of which n_v was the most sensitive, whereas the parameters k_s, α, θ_s, and θ_r were relatively less sensitive to the temperature field.

Keywords Water temperature · Riparian zone · HYDRUS-2D · Lu et al. (2007) model · Sensitivity analysis

Introduction

The construction of dams on rivers is the most commonly used engineering measure to further the exploitation and utilization of water resources. However, dams change the water environment of the natural river, particularly water temperature. Diversion of reservoir water for power generation is mainly through release from the low-temperature hypolimnion (Harleman 1982), and this released low-temperature water is used for agricultural irrigation, and ecological water requirements. Lateral hyporheic exchange with the released low-temperature water results in changes to natural water temperature and moisture of the riparian zone hyporheic layers (Curry et al. 1994; Boutt and Fleming 2009; Nowinski et al. 2012), thereby negatively impacting the environment, including animal communities, crop growth and soil respiration (Mark et al. 2012; Laganière et al. 2012), which is detrimental to the sustainable and healthy development of rivers.

Past studies on water flow and thermal dynamics of the riparian zone mostly focused on the vertical exchange between the riverbed and surface water (Arntzen et al. 2006; Fritz and Arntzen 2007; Gerecht et al. 2011). For example, Giraldo et al. (2011) established a two-dimensional temperature and seepage field coupled model of surface water–groundwater interactions and found that the temperature distribution in shallow aquifers in the riparian zone hyporheic layers was significantly affected by heat transfer in the unsaturated zone. Vogt et al. (2012) continuously

✉ Jie Ren
renjie@xaut.edu.cn; happy2006cn@163.com

1 State Key Laboratory of Eco-hydraulics in Northwest Arid Region of China, Xi'an University of Technology, Xi'an 710048, Shaanxi, China

2 State Key Laboratory of Hydrology-Water Resources and Hydraulic Engineering, Hohai University, Nanjing 210098, Jiangsu, China

3 Changjiang River Scientific Research Institute, Wuhan 430010, Hubei, China

4 College of Water & Architectural Engineering, Shihezi University, Shihezi 832000, Xinjiang, China

Published online: 16 April 2019

observed the temperature of shallow groundwater in the riparian zone by use of a distributed optical fiber temperature sensor (DTS). By analyzing the temperature of the vertical section, they identified an uneven spatial distribution of groundwater temperature in the riparian zone which varied with the depth of groundwater flow velocity. The release of low-temperature water from a reservoir into a downstream channel will influence the riparian hyporheic zone, the dynamics of lateral hyporheic exchange and the heat transfer mechanism. A study of the water temperature of the Sauce Grande River in Argentina by Casado et al. (2013) found that the natural water temperature dynamics experienced a significant delay and reduction in peak due to the influence of low-temperature water released from a reservoir. Although there have been some studies on hyporheic exchange and temperature distribution within the riparian zone downstream of a dam, these studies have been field based and relatively costly to conduct. Further studies are hindered by the lack of an effective hydro-thermal coupling model; therefore, further attempts are required to identify a suitable model coupling approach.

The temperature distribution of the unsaturated zone is a research priority within many disciplines. Hydrogeology usually only considers the seepage heat transfer process of the saturated zone, whereas soil science limits study to heat transfer of the unsaturated zone. However, the seasonal fluctuations of the temperature distribution of the unsaturated zone are affected by unsaturated seepage; therefore, it is necessary to consider the heat transfer processes of both the saturated and unsaturated zones. In applied research, such as temperature tracing within shallow geological bodies (Xu et al. 2015) or seepage monitoring of hydraulic structures (Alekseevich and Sergeevich 2017; Yosef et al. 2017), the observation of temperature in the unsaturated zone is necessary as temperature in the unsaturated zone can reflect the temperature influences of surface water–groundwater interactions. At the same time, the unsaturated zone will be affected by atmospheric temperature. Therefore, a saturated–unsaturated seepage model must be established to effectively describe actual seepage.

The increased used of computer technology has facilitated the use of the soil hydro-thermal dynamic equation. HYDRUS-2D is a commercial software package developed by an international groundwater simulation center in 1999 (Šimůnek et al. 1999). The software is widely used for the study of soil water flow and provides a modeling environment for the analysis of water flow and solute transport in variably saturated porous media. The two-dimensional finite element model HYDRUS-2D for simulating water movement, heat, and multiple solutes in variably saturated media is included in the software. Many previous studies applied HYDRUS to analyze soil hydro-thermal migration (Wang et al. 2013; Zhao et al. 2018). Saito et al. (2006) develop a numerical model within the HYDRUS code to solve the coupled equations governing liquid water, water vapor, and heat transport, together with the surface water and energy balance. Brunetti et al. (2017) used HYDRUS to establish a computationally efficient model for simulating the movement of water, heat and multiple solutes in variably saturated porous media. Brunetti et al. (2018) applied HYDRUS-2D to assess the impact of different soil properties on the thermal and hydraulic behavior of a hypothetical green roof.

COMSOL Multiphysics is used to simulate physical processes by solving partial differential equations (groups) based on finite element analysis and is widely used in a variety of physical fields such as fluid mechanics, heat conduction, structural mechanics and electromagnetic analysis. Shao et al. (2014) used the software to couple a dual-permeability model with a soil mechanics model for the evaluation of landslide stability at hillslope scales up to 100 m. Oosterbaan et al. (2016) used the software to create a model in which heat propagation through rock surrounding a rock pit was simulated and compared with measured data. Ho and Dickson (2017) employed the COMSOL finite element code to conduct numerical analysis of heat collection pipes in a heat collection system to simplify the complex heat transfer mechanisms associated with heat extraction. Liu and Yu (2011) used the software to develop a coupled multiphysics simulation model to investigate the behaviors of porous materials under frost action and established a theoretical framework to formulate the coupled thermo-hydro-mechanical processes in freezing porous materials. Wu and Song (2015), based on the characteristics of the temperature distribution of an earth rockfill dam, used the software to establish a coupled mathematical model of the saturated–unsaturated seepage and temperature fields.

The purpose of the present study was to compare the differences in simulations of the temperature distribution of the riparian zone between the Lu et al. (2007) model based on COMSOL Multiphysics and the Horton thermal conductivity model (Chung and Horton 1987) based on HYDRUS-2D by numerical simulation and a laboratory test. The present study also aimed to provide a numerical method for studying the hydro-thermal dynamics of low-temperature water infiltration into the riparian zone. There are many parameters associated with the hydro-thermal coupling model of the riparian zone, resulting in a large workload for model calibration. A sensitivity analysis was conducted using the orthogonal test analysis method to conserve computing resources by quantitatively analyzing the influence of various factors on the model so as to identify the main factors driving the temperature distribution. More attention was then placed on the accurate representation of these factors in the model.

Materials and methods

Laboratory investigations

The experimental facility consisted of a water storage tank, a water table control console, a hydro-thermal box for alternating temperatures and a sand tank (Fig. 1a). The water storage tank contained a cooling and heating system to control the temperature of the outflow. Water flowed from the water storage tank, forming a steady flow and water head, flowing to the sand tank through the water table control console. The sand tank was made of plexiglass with a total length of 80 cm. The sand tank was separated into a reservoir inflow and reservoir outflow chamber by a plexiglass baffle. The sediment-filled section was 60 cm in length, 20 cm wide and 80 cm in height. Water flow in the tank was horizontal (Fig. 1b). The inlet and outlet featured perforated plates and gauze to ensure uniform flow across the entire cross-section without losing sediment. The perforated plates located at the upstream end minimized pulsing action and facilitated a smooth flow of water into the study section. The inflow chamber contained two overflow holes of 30 cm and 50 cm in height. The outflow chamber contained one overflow hole of 5 cm in height. Before each infiltration test, the hydraulic head was stabilized at an initial level of 30 cm from the inflow chamber of the sand tank. The sand tank was equipped with a heating and cooling system to reduce heat exchange with the environment. During alternations of temperature in the hydro-thermal box, a solar radiation simulation board was used to simulate radiation conditions. In all experiments, air-dried sand was used as the sample (50th percentile grain diameter $D_{50}=0.68$ mm the uniformity coefficient Cu = 0.5) with an average bulk density of 1560 kg/m^3, and moisture content of 0.02 m^3/m^3. The initial temperature of the sample was maintained at 20 °C for over 24 h by use of the hydro-thermal box.

A constant infiltration water temperature was applied to all experiments. The tests were performed for three different water temperatures (4.0 °C, 6.0 °C and 9.5 °C), two different hydraulic heads (25 cm and 45 cm) and two different radiation temperatures (no radiation and 22 °C). The summary of the experiment conditions is given in Table 1. The data were uploaded to a computer every 1 min using the 30 temperature sensors throughout the three tests. The positions of the 30 temperature sensors are shown in Table 2. Measurements were taken at six different heights at each location: (1)

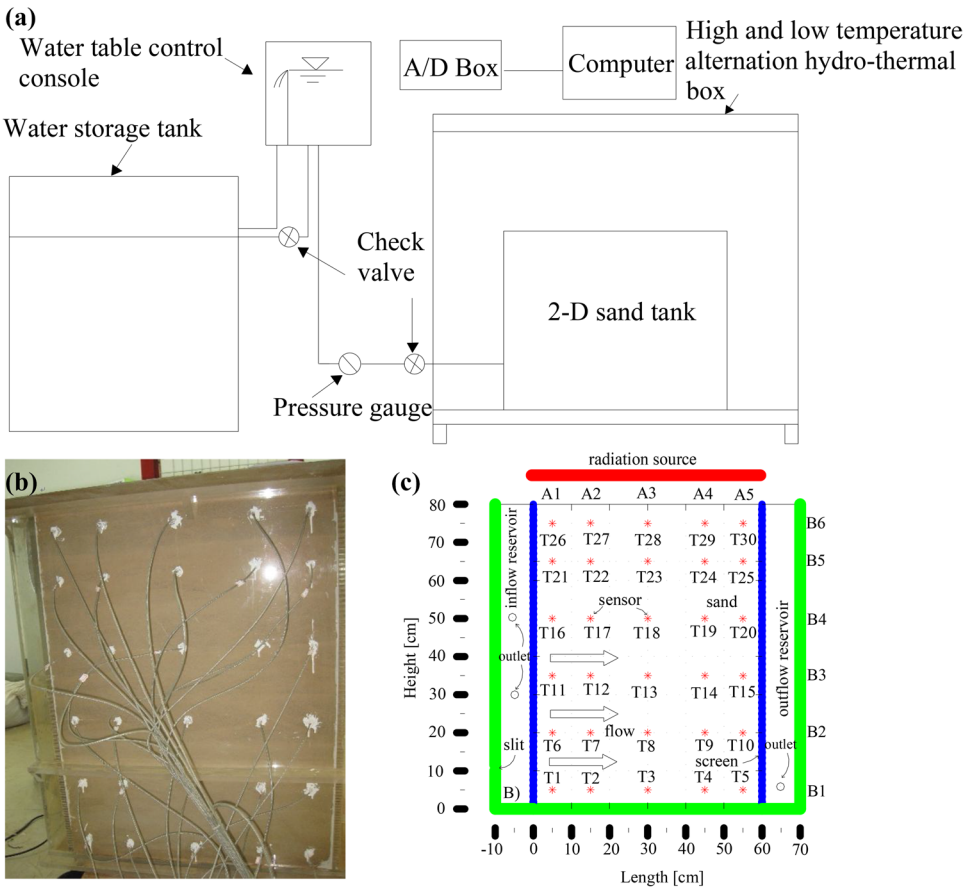

Fig. 1 View of the experimental tank setup [modified from Ren et al. (2018)]: **a** Schematic presentation of the temperature heating/cooling system, **b** photograph of 30 temperature sensors placed in the sand tank and **c** scheme showing the layout of the temperature sensors in the sand tank

Table 1 Experimental plan

	Water temperature (°C)	Hydraulic head (cm)	Radiation (°C)	Duration (min)
Condition 1	9.5	25	NA	500
Condition 2	4.0	25	22	500
Condition 3	6.0	45	22	500

5 cm below the surface (T26, T27, T28, T29 and T30); (2) 15 cm below the surface (T21, T22, T23, T24 and T25); (3) within the mid sand profile 30 cm below the surface (T16, T17, T18, T19 and T20); (4) 50 cm below the surface (T11, T12, T13, T14 and T15); (5) near the bottom 60 cm below the surface (T6, T7, T8, T9 and T10) and; (6) 75 cm below the surface (T1, T2, T3, T4 and T5), as shown in Fig. 1c. Further details on the experimental facility and methods are provided by Ren et al. (2018).

Model description

The saturated–unsaturated transient seepage field of the riparian zone is described by the Richard's equation:

$$\rho_w\left(\frac{C_m}{\rho_w g}+S_e S_s\right)\frac{\partial p}{\partial t}+\nabla\rho_w\left(-\frac{k_s k_r(\theta)}{\mu(T)}\nabla(p+\rho_w g z)\right)=Q_m \tag{1}$$

where ρ_w is the density of water (kg/m^3), C_m is the specific moisture capacity (1/m), g is the gravity acceleration (m/s^2), S_e is the relative degree of saturation, S_s is the elastic water storage rate (1/Pa), p is the pressure (Pa), ∇ is the Laplacian operator, θ is the moisture content (%), k_s is the media saturated hydraulic conductivity (m/s), $k_r(\theta)$ is the unsaturated zone relative hydraulic conductivity ($0 \le k_r(\theta) \le 1$), and is a function of the moisture content θ, $\mu(T)$ is the dynamic viscosity of water (Pa s), where $\mu(T)=0.00002414\times10^{(247.8/(T+133.16))}$ (Kipp 1987) and is a function of temperature, z is the vertical coordinate (upwards is positive) and Q_m is the water source.

Some studies have proposed empirical formulae to describe the characteristics of soil moisture in unsaturated zones. Typical examples are models by van Genuchten (1980), Brooks–Corey (Milly 1987) and Gardner (Milly 1987; Gardner et al. 1970). Among these, the van Genuchten model is characterized by a high accuracy, a physical process representation and strong applicability. This model is widely used, suitable for almost all soil texture types and the fitted curve can be completely characterized for the dry, transition and saturation sections of soil. Therefore, the present study selected the van Genuchten model, which can be expressed as:

$$\theta=\theta_r+S_e(\theta_s-\theta_r) \tag{2}$$

$$S_e=1/(1+(\alpha h_p)^{n_v})^m \tag{3}$$

$$C_m=\frac{\alpha m}{1-m}(\theta_s-\theta_r)S_e^{1/m}(1-S_e^{1/m})^m \tag{4}$$

$$k_r=S_e^{1/2}[1-(1-S_e^{1/m})^m]^2 \tag{5}$$

Here, θ_r is the residual water content (m^3/m^3), θ_s is the saturated water content (m^3/m^3), α is the reciprocal of the water characteristic curve intake (1/m), h_p is the hydraulic pressure head (h_p=p_w/$\rho_w g$), which in the unsaturated zone is equal to the negative pressure head h_c (m) and n_v is an indicator of the slope of the water characteristic curve, obtained by fitting the soil moisture characteristic curve, $m=1-1/n_v$.

The saturated–unsaturated heat transfer model can be expressed by the following equation (Healy and Ronan 1996):

$$\frac{\partial(\rho_{eq}c_{eq}T)}{\partial t}=\nabla(\lambda_{eq}\nabla T)+\nabla(\theta\rho_w c_w D_H\nabla T)-\nabla(\theta\rho_w c_w uT)+Q_s \tag{6}$$

where ρ_{eq} is the effective density (kg/m^3), c_{eq} is the effective specific heat capacity (J/(kg °C)), T is the temperature (°C), t is the time (s), λ_{eq} is the effective thermal conductivity (W/(m °C)), c_w is the volumetric heat capacity of water (J/(kg °C)), D_H is the hydrodynamic dispersion coefficient, u is the average water velocity (m/s), and Q_s is the heat source.

Table 2 Location of temperature sensors

Point	T1	T2	T3	T4	T5	T6	T7	T8	T9	T10	T11	T12	T13	T14	T15
x (cm)	5	15	30	45	55	5	15	30	45	55	5	15	30	45	55
y (cm)	5	5	5	5	5	20	20	20	20	20	35	35	35	35	35
Point	T16	T17	T18	T19	T20	T21	T22	T23	T24	T25	T26	T27	T28	T29	T30
x (cm)	5	15	30	45	55	5	15	30	45	55	5	15	30	45	55
y (cm)	50	50	50	50	50	65	65	65	65	65	75	75	75	75	75

The symbol x indicates the horizontal distance from the left screen boundary whereas y indicates the vertical distance from the bottom (Fig. 1c)

$$D_{Hij} = \alpha_T |v| \sigma_{ij} + (\alpha_L - \alpha_T) v_i v_j |v| \quad (7)$$

where α_T is the lateral dispersion (m), α_L is the vertical dispersion (m), v_i is the velocity vector in the i direction, δ_{ij} is the kriging constant, which is 1 when $i=j$ and 0 otherwise and $|v|$ is the value of the velocity vector.

The effective density and effective specific heat capacity of rock and soil follow the law of volume average, namely:

$$\rho_{eq} = (1-n)\rho_s + \theta\rho_w + (n-\theta)\rho_g \quad (8)$$

$$c_{eq} = (1-n)c_s + \theta c_w + (n-\theta)c_g \quad (9)$$

where the subscripts s, w and g represent the sand, water, and air, respectively, n is the porosity of the porous medium (%) and $\theta=n$ when it is in an saturated state.

Soil thermal conductivity model

Soil effective thermal conductivity ($\lambda_{eq}(\theta)$) describes the thermal conductivity of multiphase soils at a unit temperature gradient. The effective thermal conductivity of soil is the key parameter used in geotechnical engineering for heat transfer analysis, and its size will vary with the spatial distribution of soil water content. A change in temperature will affect the water viscosity and pore structure of soil, which would consequently affect the heat conduction process. Therefore, soil thermal conductivity has received widespread attention both in China and abroad, resulting in the development of several calculation models.

In HYDRUS-2D, the soil thermal conductivity model uses the previously widely used Horton thermal conductivity model (Chung and Horton 1987), which can be expressed as:

$$\lambda_{eq}(\theta) = b_1 + b_2\theta + b_3\theta^{0.5} \quad (10)$$

where b_1, b_2 and b_3 are empirical parameters specified for each soil texture (coarse, medium and fine). In the present study, the values b_1, b_2 and b_3 (W/(m °C)) were chosen from the HYDRUS-2D default values, namely 4,924,810, − 51,969,500 and 106,034,000, respectively.

With the development of a soil thermal conductivity model, a more accurate and practical model was developed. Lu et al. (2007) proposed an equation for the relationship between normalized thermal conductivity and saturation ($K_e - S_r$) over the entire range of soil water content. Compared with previous thermal conductivity models, the model by Lu is able to more accurately predict soil thermal conductivity. Therefore, this model was used in COMSOL Multiphysics to calculate the equivalent thermal conductivity $\lambda_{eq}(\theta)$ of unsaturated soils.

The Lu et al. (2007) model is based on saturation to interpolate the thermal conductivity of dry soil (λ_{dry}) and the saturated soil (λ_{sat}) to obtain the thermal conductivity of unsaturated soil:

$$\lambda_{eq}(\theta) = (\lambda_{sat} - \lambda_{dry})K_e + \lambda_{dry} \quad (11)$$

where λ_{dry} and λ_{sat} are calculated as follows:

$$\lambda_{dry} = -0.56n + 0.51 \quad (12)$$

$$\lambda_{sat} = \lambda_s^{1-n}\lambda_w^n \quad (13)$$

where λ_s is the thermal conductivity of soil obtained from the quartz content (q) and its thermal conductivity (λ_q=7.7 W/(m °C)) and the thermal conductivity of other minerals (λ_0), i.e., $\lambda_s=\lambda_q^q\lambda_0^{1-q}$. Among them: λ_0=2.0 W/(m °C) ($q>0.2$); λ_0=3.0 W/(m °C) ($q\le0.2$) and λ_w is the thermal conductivity of water (W/(m °C)).

For conventional soil, the normalized thermal conductivity K_e is

$$K_e = \exp\left\{\alpha[1 - S_r^{(\alpha-1.33)}]\right\} \quad (14)$$

where S_r is the degree of saturation, α is a soil texture-dependent parameter and the values of sand, loam and clay are 1.05, 0.9 and 0.58, respectively. The value 1.33 is a shape parameter.

Boundary conditions and parameters settings

Based on the above numerical model, the finite element solution of the coupled model for representing the saturated–unsaturated seepage field and temperature field was realized by modifying the related modules in HYDRUS-2D and COMSOL Multiphysics, respectively. As shown in Fig. 2, the domain geometry was rectangular, and measured 60 cm wide and 80 cm deep. A homogeneous and isotropic soil texture throughout the domain was assumed.

The Galerkin finite element method was used in HYDRUS-2D to solve the governing water flow and heat flow equations, thereby allowing the numerical solution of the transport domain to be obtained. The infiltration head extended to 30 cm in a relatively short period of time (a few seconds) during the low-temperature water application. Therefore, the left infiltration boundary (DE) was assumed to be a constant head boundary condition, and the infiltration line was assumed to be a line source. A zero-flux boundary was used at the remaining part of the left boundary (CD) and the bottom boundary (EA). An atmospheric boundary was used at the soil surface (BC). The entire right side of the domain (AB) was assigned a variable head boundary condition with the option "Seepage Face BC when the specified nodal pressured head is negative". The soil heat regime was affected by water temperature. The left infiltration boundary (DE) and right boundary (AB) were then used as the Cauchy type boundary. The soil surface boundary (BC) was used as the Dirichlet boundary. No effect on soil surface temperature through radiation was set for Model 1, with temperature set to 20 °C. The soil surface boundaries of Models 2

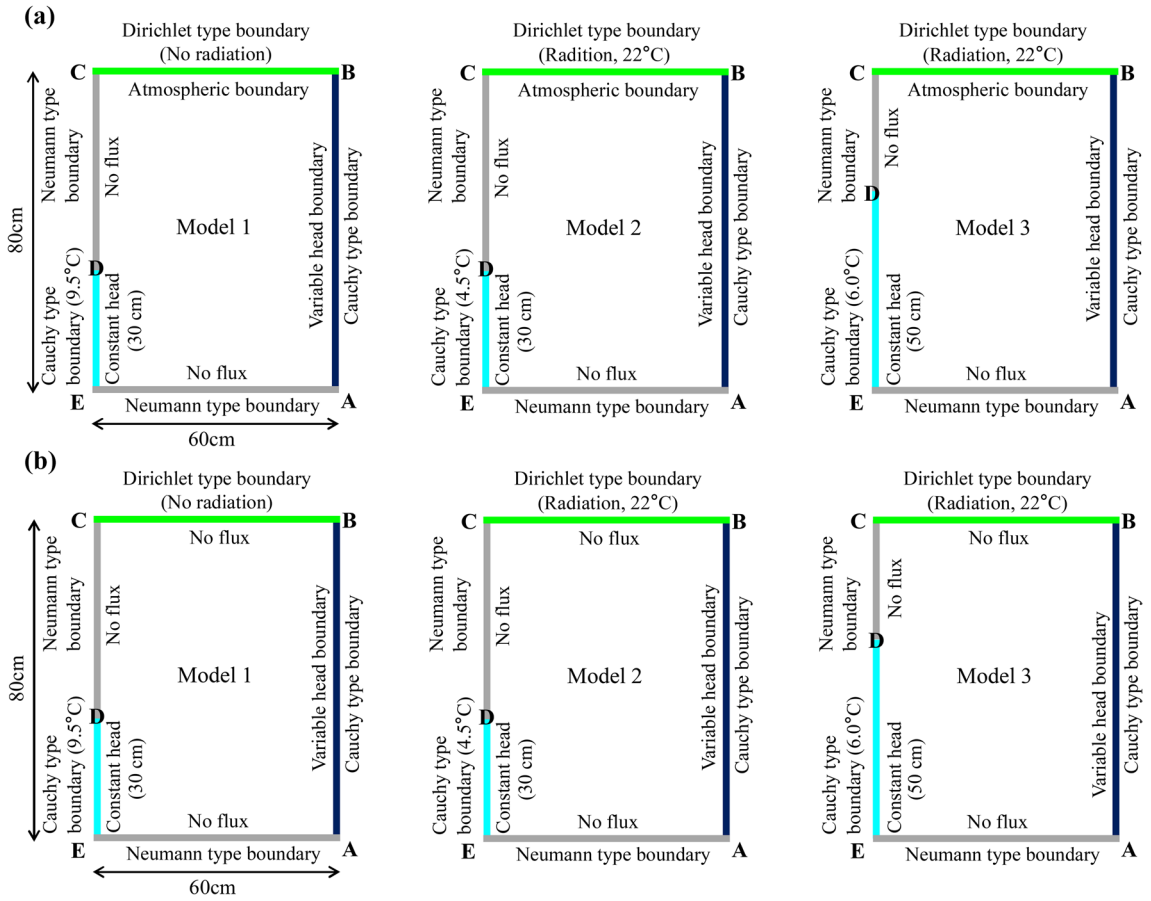

Fig. 2 Boundary conditions of the modeling scenarios for different experiments: (Model 1) Condition 1, (Model 2) Condition 2, (Model 3) Condition 3; **a** HYDRUS Model boundary conditions, **b** COMSOL Model boundary conditions

and 3 had a constant radiation temperature of 22 °C, which was controlled by the solar radiation controller system. The Neumann type boundaries were used at the remaining part of the left boundary (CD) and the bottom boundary (EA). The settings of the HYDRUS model boundary condition are shown in Fig. 2a.

Differences between the software models resulted in different boundary conditions. During the process of modeling using COMSOL, the present paper refers to the setting of the boundary conditions of the predecessors in the COMSOL hydrological modeling process. Although the boundary conditions of COMSOL are slightly different to those of HYDRUS, certain similarities exist between the two. A zero-flux boundary condition was used at the soil surface boundary (BC), because there is no "atmosphere boundary" in COMSOL. Chui and Freyberg (2007) set the soil surface boundary (BC) to a zero-flux boundary. Some boundary settings were the same for both models. The COMSOL model boundary condition setting is shown in Fig. 2b. Table 3 shows the calculated parameters of the seepage and temperature fields of the model, and the parameter values of the laboratory test and mathematical model are shown in Table 4.

Table 3 Parameters of the transient heat transfer model used to simulate the seepage and temperature fields

Parameters	Value
k_s (m/s)	8.25×10^{-5}
θ_s (m^3/m^3)	0.342
θ_r (m^3/m^3)	0.023
S_s (1/Pa)	10^{-6}
λ_g (W/(m °C))	0.024
c_g (J/(kg °C))	1005
ρ_g (kg/m^3)	1.205
n (%)	35
q (%)	50
α_T (m)	0.01
α_L (m)	0.01
c_w (J/(kg °C))	4186
λ_w (W/(m °C))	0.58
ρ_w (kg/m^3)	1000
c_s (J/(kg °C))	800
ρ_s (kg/m^3)	1560

Table 4 Laboratory test and calibration of mathematical model parameter values

	α (l/m)	n_v	θ_s (m^3/m^3)	θ_r (m^3/m^3)	k_s (m/s)
Experiment	4.2	5.2750	0.342	0.023	8.25×10^{-5}
HYDRUS-2D	3.8	5.2750	0.342	0.021	8.25×10^{-5}
COMSOL Multiphysics	1.0	1.21	0.342	0.023	8.25×10^{-5}

Model evaluation

The root mean square error (RMSE), Pearson correlation coefficient (PCC) and Nash–Sutcliffe model efficiency coefficient (NSE) were used in the present study to evaluate the accuracy of the model:

$$\mathrm{RMSE} = \sqrt{\frac{1}{m}\sum_{i=1}^{m}(T_{\mathrm{obs},i} - T_{\mathrm{model},i})^2} \tag{15}$$

$$\mathrm{PCC} = \frac{\sum_{i=1}^{m}(T_{\mathrm{obs},i} - \overline{T}_{\mathrm{obs}})(T_{\mathrm{model},i} - \overline{T}_{\mathrm{model}})}{\sqrt{\sum_{i=1}^{m}(T_{\mathrm{obs},i} - \overline{T}_{\mathrm{obs}})^2}\sqrt{\sum_{i=1}^{m}(T_{\mathrm{model},i} - \overline{T}_{\mathrm{model}})^2}} \tag{16}$$

$$\mathrm{NSE} = 1 - \frac{\sum_{i=1}^{m}(T_{\mathrm{obs},i} - T_{\mathrm{model},i})^2}{\sum_{i=1}^{m}(T_{\mathrm{obs},i} - \overline{T}_{\mathrm{obs}})^2} \tag{17}$$

where m is the number of data, $T_{\mathrm{obs},i}$ and $T_{\mathrm{model},i}$ are the ith observed and the modeled temperature, respectively, and $\overline{T}_{\mathrm{obs}}$ and $\overline{T}_{\mathrm{model}}$ are the equivalent observed and modeled mean temperatures, respectively. The RMSE can vary from 0 to $+\infty$. A smaller RMSE indicates a better model fit to observed data. The PCC ranges from -1 to 1, with higher values indicating better model congruence. A correlation coefficient value in the ranges of 8–1.0, 0.6–0.8 and 0.4–0.6 indicates an extremely strong, strong and moderate relationship, respectively. The NSE ranges from $-\infty$ to 1, and can be used to access the predictive power of hydrological models, with a value closer to 1.0 indicating a better match between observed and modeled values. NSE values > 0.6 and 0 indicate a good prediction and a prediction no better than taking the average of the observed data, respectively.

Result and discussion

Model calibration

Figure 3 shows the simulated and measured temperature versus time curves at various points in the longitudinal profile at different locations along the infiltration boundary based on COMSOL Multiphysics and HYDRUS-2D. The model calibration accuracies are expressed by RMSE, PCC and NSE values listed in Table 5. Table 5 shows that the COMSOL Multiphysics RMSE varied between 0.13 and 1.39 °C with an average of 0.67 °C, and a relatively small deviation between the simulated and observed values. Correlations were expressed by PCC. The results showed that the simulated values at all observation points were strongly correlated with the measured values (|PCC| > 0.6 accounts for 100% of observations). Among them, extremely strong correlations were obtained for 81.82% of observation points (|PCC| > 0.8). The NSE showed that 63.64% of observation points had a good agreement between simulated and experimental values (NSE > 0.6). Among them, the observation points (T20, T21, T23, T24, T25, T26, T27 and T28) located on the soil surface showed poor model matching. The HYDRUS-2D RMSE ranged from 0.26 to 1.99 °C with an average of 0.88 °C. Correlations to observed data obtained with the HYDRUS-2D were similar to that obtained through COMSOL with strong and extremely strong correlations obtained for 100% and 81.82% of observation points, respectively. A total of 54.55% of observation points showed a good agreement between simulated and experimental values (NSE > 0.6), whereas a low degree of matching was obtained for the soil surface observation points. Therefore, the present study found the use of COMSOL based on the Lu et al. (2007) model to be relatively more accurate.

Model verification

The present study verified whether the Lu et al. (2007) model based on COMSOL is able to characterize the dynamic changes in temperature in the riparian zone when exposed to low-temperature water discharged by a dam. Figures 4 and 5 represent Condition 2 and Condition 3 based on COMSOL and HYDRUS used to simulate the dynamic changes in the riparian zone by dam discharge of cold water, and the model verification results are listed in Tables 6 and 7. Under Condition 2, the RMSE of the COMSOL simulation varied from 0.21 to 3.32 °C with an average of 1.26 °C. The RMSE of the T12 observation point was 3.32 °C with a relatively large error. Strong and extremely strong correlations were obtained for 90.91% (|PCC| > 0.6), and 81.82% (|PCC| > 0.8), respectively. The RMSE of the HYDRUS simulation results varied from 0.36 to 2.75 °C with an average of 1.41 °C. Similar to the COMSOL result, the error of the T12 observation point was larger. Strong and extremely strong correlations

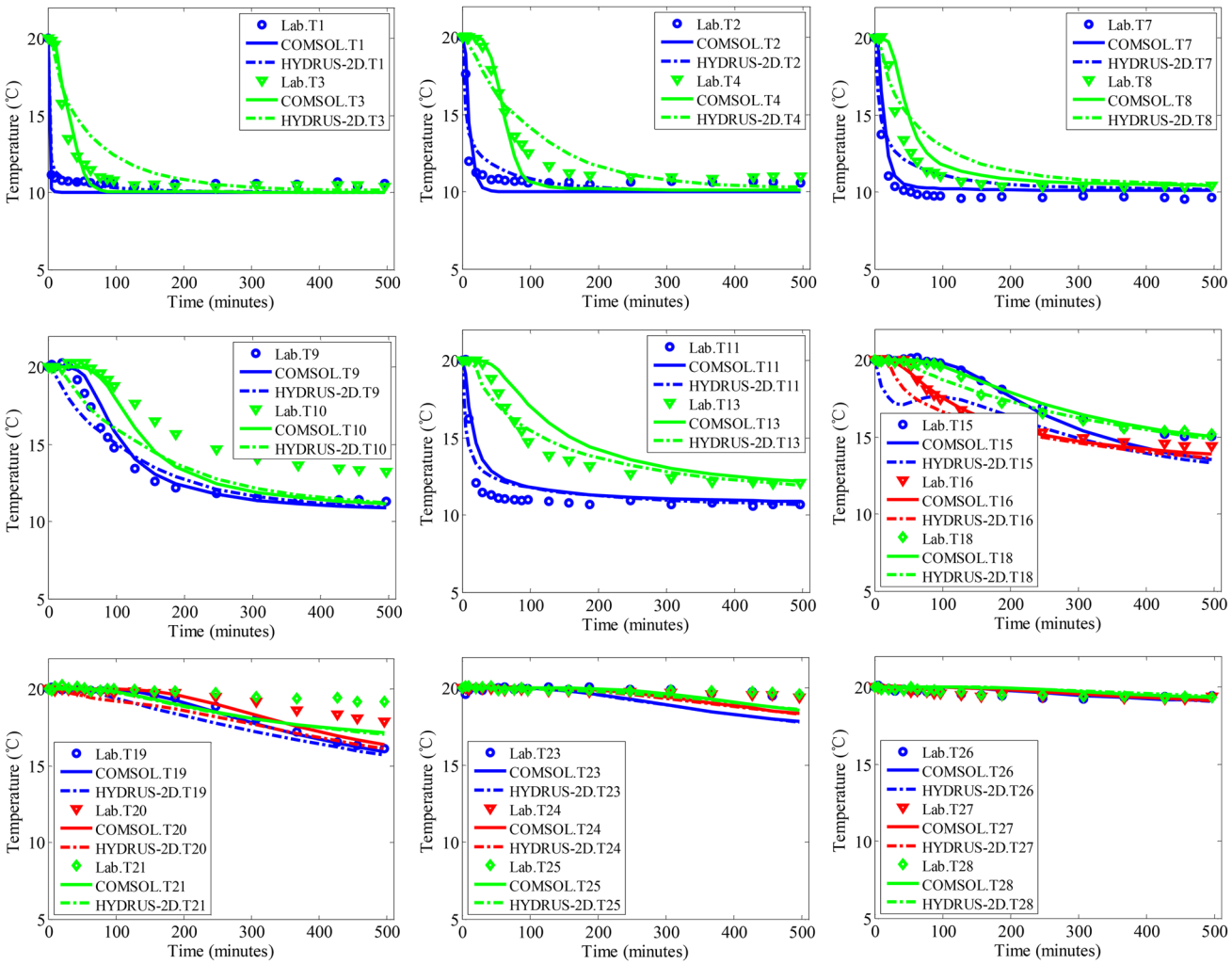

Fig. 3 Comparison of measured and simulated temperature time series at different observation points under Condition 1. The symbols show measured data under Condition 1 and curves show numerical modeling results

were obtained for 95.45% and 86.36% of observation points, respectively. Good matches were obtained for 77.27% of the observation points (NSE > 0.6). The PCC and NSE values of HYDRUS under Condition 2 were better than those of COMSOL, whereas the RMSE was a little worse. Under Condition 3, The COMSOL RMSE varied from 0.37 to 2.28 °C with an average of 1.09 °C, and strong correlations accounted for 95.24% of observation points. Good matches were obtained for 85.71% of the observation points. The RMSE of the HYDRUS simulation results varied from 0.41 to 4.92 °C with an average of 1.63 °C. Compared with other observations, the RMSE value was larger at T10 and T19, indicating that the simulation error was larger. Correlation analysis results showed that the simulated values of all observation points were extremely strongly correlated with the measured values. The model efficiency results showed that 71.42% of the observation points matched well with the measured values.

These results showed that the Lu et al. (2007) model based on COMSOL and the Horton thermal conductivity model based on HYDRUS each had their own advantages, thereby making it difficult to evaluate which method performed the best within the present study. Therefore, we used the global analysis method to compare the simulations between COMSOL and HYDRUS for all the observation points under different domain conditions. The results shown in Figs. 6 and 7 compare the RMSE, PCC and NSE values between the two models under different domain conditions. As is evident in Fig. 7, the Lu et al. (2007) model based on COMSOL performed better than the Horton thermal conductivity model based on HYDRUS. Therefore, we used the Lu et al. (2007) model based on COMSOL to study the hydro-thermal dynamics of the riparian zone.

Table 5 Root mean square error (RMSE; °C), Pearson correlation coefficient (PCC) and Nash–Sutcliffe model efficiency coefficient (NSE) values for COMSOL Multiphysics and HYDRUS-2D model calibration under Condition 1

Temperature sensors	COMSOL multiphysics			HYDRUS-2D		
	RMSE (°C)	PCC	NSE	RMSE (°C)	PCC	NSE
T1	0.60	0.998	0.912	0.40	0.985	0.961
T2	0.85	0.942	0.879	0.90	0.935	0.867
T3	0.70	0.971	0.955	1.37	0.932	0.829
T4	0.93	0.994	0.936	0.98	0.966	0.929
T7	0.81	0.983	0.931	1.51	0.936	0.762
T8	1.24	0.968	0.876	1.37	0.960	0.849
T9	0.69	0.987	0.962	0.92	0.976	0.932
T10	1.39	0.997	0.744	1.99	0.958	0.484
T11	1.08	0.965	0.858	1.30	0.914	0.797
T13	1.27	0.962	0.834	0.64	0.983	0.958
T15	0.59	0.997	0.906	1.92	0.930	− 0.035
T16	0.26	0.995	0.985	0.84	0.970	0.850
T18	0.34	0.989	0.967	0.36	0.984	0.962
T19	0.13	0.997	0.990	0.52	0.971	0.853
T20	0.64	0.992	0.061	0.97	0.972	− 1.111
T21	0.99	0.949	− 9.559	1.02	0.950	− 10.16
T23	0.74	0.763	− 16.97	0.75	0.761	− 17.28
T24	0.41	0.917	− 5.020	0.42	0.933	− 5.234
T25	0.39	0.753	− 6.535	0.39	0.801	− 6.473
T26	0.25	0.761	− 0.016	0.27	0.719	− 0.172
T27	0.27	0.782	− 0.230	0.29	0.752	− 0.368
T28	0.23	0.809	− 0.037	0.26	0.789	− 0.217

To further clarify the dynamic changes in temperature in the riparian zone, Fig. 8 shows the temperature and contour maps of the infiltration of cold water into the riparian zone at a head of 30 cm and the temperature of 9.5 °C. It can be seen from Fig. 8 that heat transfer and exchange in the aquifer of the riparian zone were affected by cold water discharge from the reservoir, which resulted in change to the temperature distribution in the riparian zone. The aquifer contained a significant vertical temperature stratification, which formed the non-isothermal environment of the low-temperature water layer and the upper natural temperature surface bidirectional radiation, with the gradient gradually decreasing with depth. The riparian zone can be divided into low, medium and high temperature zones along the horizontal direction from the near shore to the far shore. The temperature zones changed over time, demonstrating the phenomenon of cold water spreading, resulting in a gradual decrease in the gradient. The comparison of five different time periods found that the area of low temperature along the riparian zone gradually increased over time, which illustrated the rapid invasion of the riparian zone by low-temperature water.

The temperature of the soil near the infiltration level quickly equalized with that of the river at the beginning of infiltration, which increased over time. With an increase of infiltration time, the internal saturation of the riparian zone increased and the range of low temperature gradually expanded across the entire riparian zone. The surface soil temperature also changed during the first 30 min of infiltration. Between 30 and 180 min, the soil temperature below the infiltration head reached the infiltration water temperature. After 180 min, the soil temperature above the infiltration head also gradually decreased, moving toward the infiltration water temperature, and the low-temperature region also gradually increased. Due to the effect of the infiltration head, the low-temperature area of the higher water head was larger than that of the low water head.

From Fig. 8, it is evident that the initial temperature of sand was 20 °C. The points T1, T2, T3, T4, T5, T6, T7, T8, T9 and T10 near the infiltration boundary and the bottom boundary decreased rapidly and reached a steady state within the first 180 min, with temperature close to the infiltration water temperature. In contrast, more time was required for the temperatures near the upper and right boundary points to reach a steady state. With an increase in infiltration time, the temperature gradient in the low, medium and high temperature zones decreased, and the vertical stratification became more obvious.

Sensitivity analysis

Sensitivity analysis was used to identify the major factors affecting the output of the model, thereby facilitating improved model prediction. Either single factor or

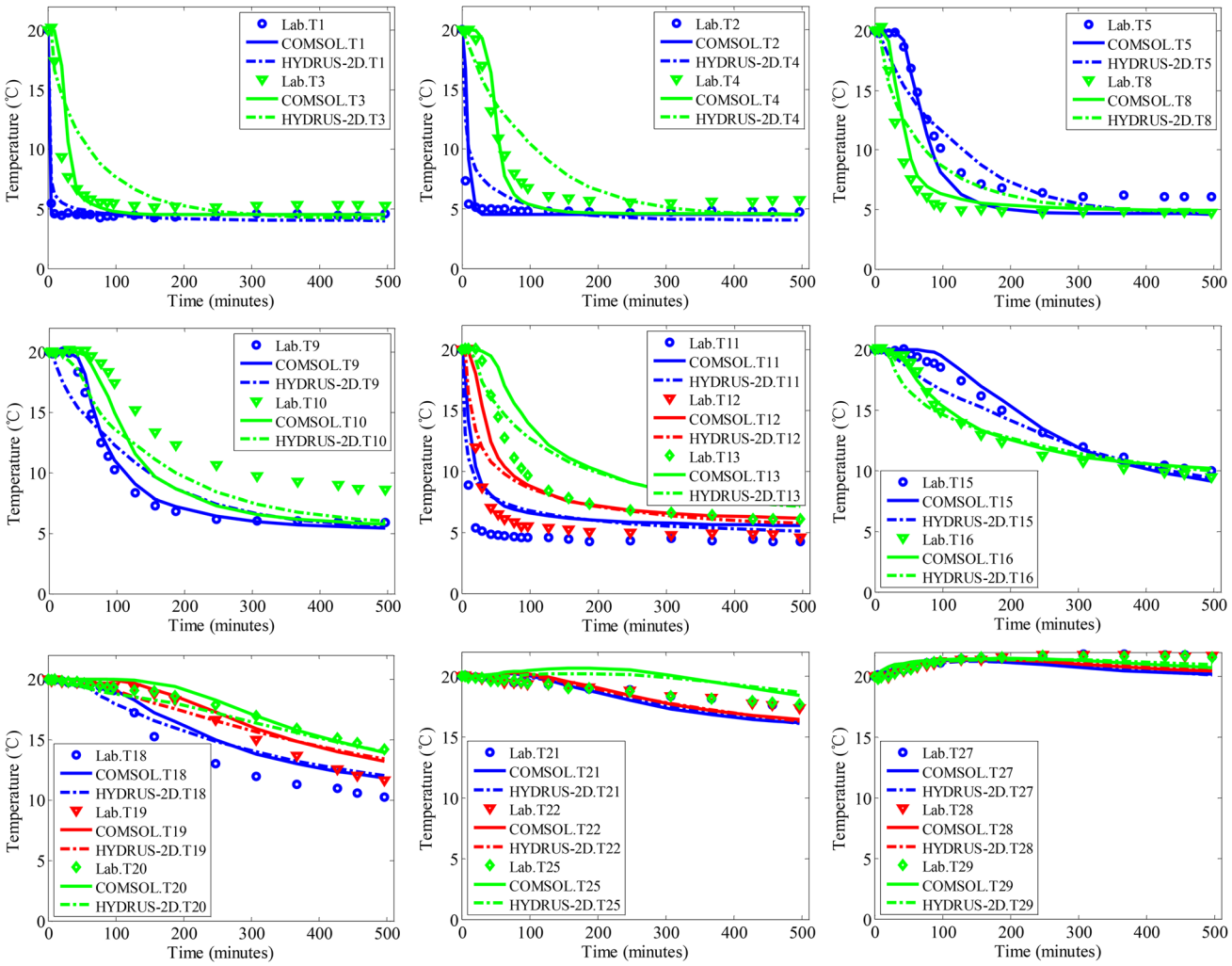

Fig. 4 Comparison of measured and simulated temperature time series at different observation points under Condition 2. The symbols show measured data under Condition 2 and curves show numerical modeling results

multi-factor sensitivity analysis can be improved. Single factor sensitivity calculation is simple and quick. However, the calculation workload would become too heavy if a comprehensive test portfolio is to be performed. On the other hand, the orthogonal test design allows for multi-factor test to seek the optimal combination. Therefore, the present study used the orthogonal test design for analysis of the sensitivity of the model.

Orthogonal design is a statistical method that arranges multi-factor experiments using a set of ready-made tables. The method assists in the statistical analysis of the results. A suitable orthogonal table was first selected and recorded as $Ln(r^m)$, where L is the symbol of the orthogonal table, r is the number of factors, n is the number of orthogonal table rows and m is the orthogonal table column number. The factors were randomly placed in the table above the column, termed the header design. The calculation scheme was determined by the orthogonal table $Ln(r^m)$ at the given level of each factor. Finally, according to the test designed by the orthogonal table, the index value of each test was calculated and the sensitivity of each factor to the index was determined according to the test result. In the present study, the results of the orthogonal test were analyzed using range analysis.

Suppose A and B represent the different factors in the experiment, r is the number of factor levels, A_i represents the ordinal values of factor A, $i=1, 2, \ldots, t$, X_{ij} represents the ordinal values of factor j, ($i=1, 2, \ldots, n$, $j=A, B, \ldots$) and n tests were performed at X_{ij} to obtain n tests results Y_k, ($k=1, 2, \ldots, n$). The formula is:

$$K_{ij} = \frac{1}{t}\sum_{k=1}^{t} Y_k - \overline{Y} \tag{18}$$

where K_{ij} is the average value of each test result of factor j at level i, t is the number of trials for factor j at level i, k is the kth test index value, $\overline{Y}$ is the average of all test results.

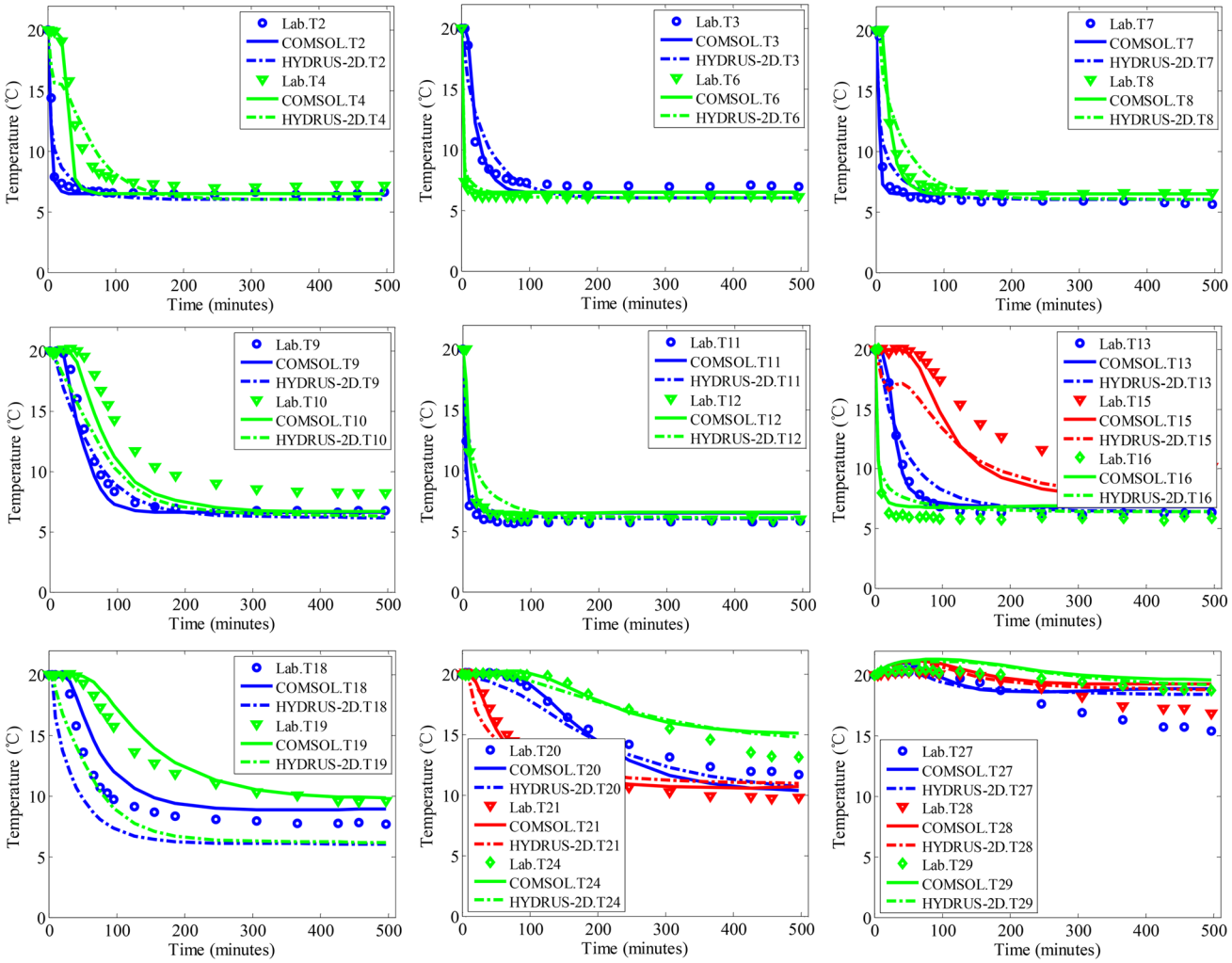

Fig. 5 Comparison of measured and simulated temperature time series at different observation points under Condition 3. The symbols show measured data under Condition 3 and curves show numerical modeling results

The criteria for evaluation of the range sensitivity method were the range values R_j for each factor, which is defined as the difference between the maximum and minimum values of the statistical parameter K_{ij} calculated at each level of this factor. The formula is:

$$R_j = \mathrm{Max}\{K_{1j}, K_{2j}, \ldots\} - \mathrm{Min}\{K_{1j}, K_{2j}, \ldots\} \quad (19)$$

The larger the value of R_j, the greater the influence of the change in the factor on the test index.

The temperature field of the riparian zone showed spatial variation. Because of the large volume of data available, a transverse section was selected for analysis, concentrating on the parameters identified during sensitivity analysis, with only the longitudinal section analyzed. The difference between the temperature field and the rated temperature field due to changes in the parameters was determined for each finite element node, following which the average change was used to represent the change in temperature. The average temperature at 500 min was selected as the main test index for sensitivity analysis. The sensitivity analysis involved seven parameters that determine the changes in temperature in the model: (1) infiltration head (H); (2) infiltration water temperature (T); (3) hydraulic conductivity (k_s); (4) van Genuchten parameter α; (5) van Genuchten parameter n_v; (6) residual moisture content (θ_r) and; (7) saturated water content (θ_s). Three levels of factors were selected for each parameter, one acting as the reference value, and then an increase and decrease of the reference value by 10%, respectively. Table 8 shows the test factors for parameter sensitivity analysis and the levels of each factor.

It was assumed that there was no interaction among the factors of the model. The $L_{18}(3^7)$ orthogonal test table was chosen according to the test factors and the number of levels, and the first column was set to empty. The test factors were assigned to the table in turn to obtain the orthogonal test

Table 6 Root mean square error (RMSE; °C), Pearson correlation coefficient (PCC) and Nash–Sutcliffe model efficiency coefficient (NSE) for COMSOL Multiphysics and HYDRUS-2D model calibration under Condition 2

Temperature sensors	COMSOL Multiphysics			HYDRUS-2D		
	RMSE (°C)	PCC	NSE	RMSE (°C)	PCC	NSE
T1	0.21	0.998	0.996	0.71	0.980	0.956
T2	2.30	0.848	0.518	1.97	0.886	0.647
T3	1.99	0.944	0.833	2.75	0.890	0.684
T4	1.35	0.989	0.942	2.16	0.933	0.852
T5	1.26	0.999	0.952	1.58	0.967	0.924
T8	1.35	0.984	0.943	2.31	0.950	0.832
T9	0.62	0.996	0.988	1.68	0.965	0.915
T10	2.33	0.991	0.749	2.53	0.970	0.705
T11	2.54	0.945	0.702	2.63	0.901	0.681
T12	3.32	0.931	0.601	2.55	0.954	0.766
T13	2.78	0.953	0.736	1.96	0.977	0.869
T15	0.60	0.994	0.975	0.98	0.987	0.933
T16	0.46	0.997	0.986	1.09	0.974	0.927
T18	1.16	0.993	0.903	1.17	0.987	0.901
T19	0.76	0.999	0.931	0.80	0.984	0.924
T20	0.43	0.991	0.947	0.41	0.994	0.952
T21	0.74	0.971	0.147	0.68	0.978	0.283
T22	0.62	0.959	0.419	0.58	0.971	0.495
T25	1.02	0.669	− 0.872	0.87	0.775	− 0.339
T27	0.75	0.136	− 0.497	0.70	0.398	− 0.289
T28	0.66	0.362	0.048	0.51	0.691	0.428
T29	0.49	0.679	0.455	0.36	0.889	0.720

Table 7 Root mean square error (RMSE; °C), Pearson correlation coefficient (PCC) and Nash–Sutcliffe model efficiency coefficient (NSE) for COMSOL Multiphysics and HYDRUS-2D model calibration under Condition 3

Temperature sensors	COMSOL Multiphysics			HYDRUS-2D		
	RMSE (°C)	PCC	NSE	RMSE (°C)	PCC	NSE
T2	0.62	0.986	0.963	0.88	0.964	0.929
T3	0.64	0.994	0.978	1.37	0.951	0.901
T4	1.60	0.977	0.896	1.73	0.949	0.879
T6	0.37	0.999	0.984	0.41	0.993	0.981
T7	1.75	0.918	0.817	1.68	0.922	0.833
T8	0.38	0.998	0.994	1.27	0.965	0.927
T9	0.89	0.992	0.972	1.35	0.983	0.935
T10	2.00	0.982	0.838	3.07	0.958	0.618
T11	0.80	0.988	0.942	0.91	0.970	0.926
T12	0.75	0.993	0.968	1.56	0.943	0.864
T13	0.43	0.997	0.993	1.21	0.980	0.942
T15	2.25	0.989	0.691	2.94	0.976	0.476
T16	2.28	0.862	0.707	2.36	0.849	0.687
T18	1.67	0.980	0.878	3.12	0.939	0.577
T19	0.90	0.988	0.954	4.92	0.902	− 0.371
T20	0.78	0.998	0.944	0.81	0.996	0.939
T21	0.65	0.988	0.970	1.25	0.962	0.891
T24	0.78	0.983	0.906	0.76	0.983	0.911
T27	1.51	0.771	0.280	1.32	0.842	0.451
T28	1.13	0.864	0.098	0.87	0.903	0.462
T29	0.75	0.872	− 0.709	0.55	0.896	0.080

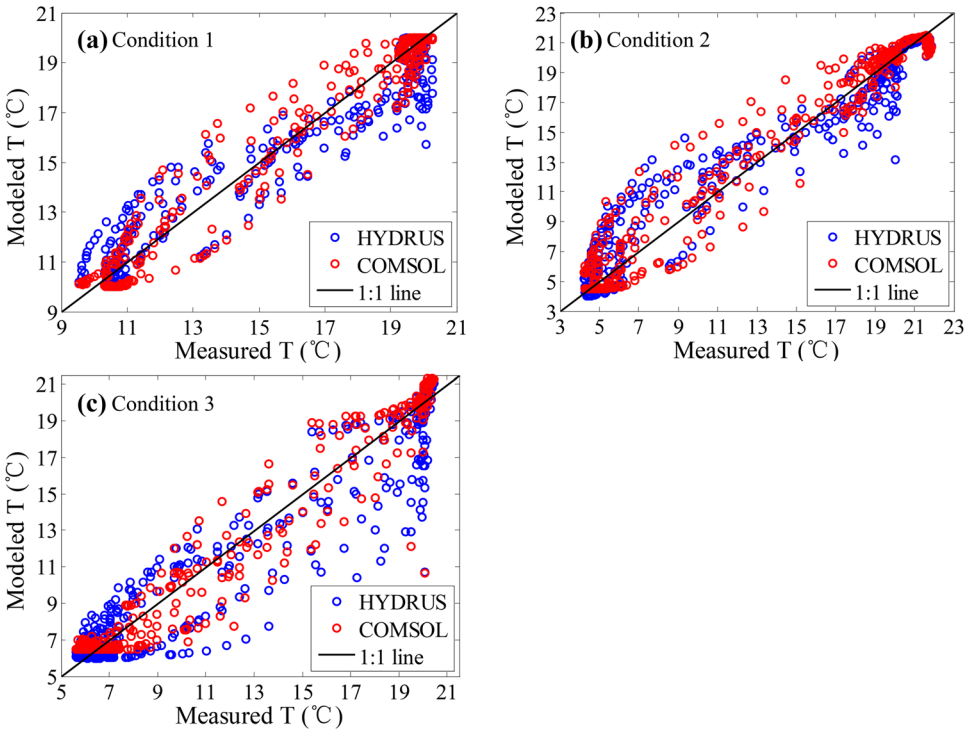

Fig. 6 A comparison of measured and modeled temperature in the domain under different conditions. The blue circle is based on the results of the COMSOL simulation using the Lu et al. (2007) model. The red circle is based on the results of the HYDRUS simulation using the Horton thermal conductivity model

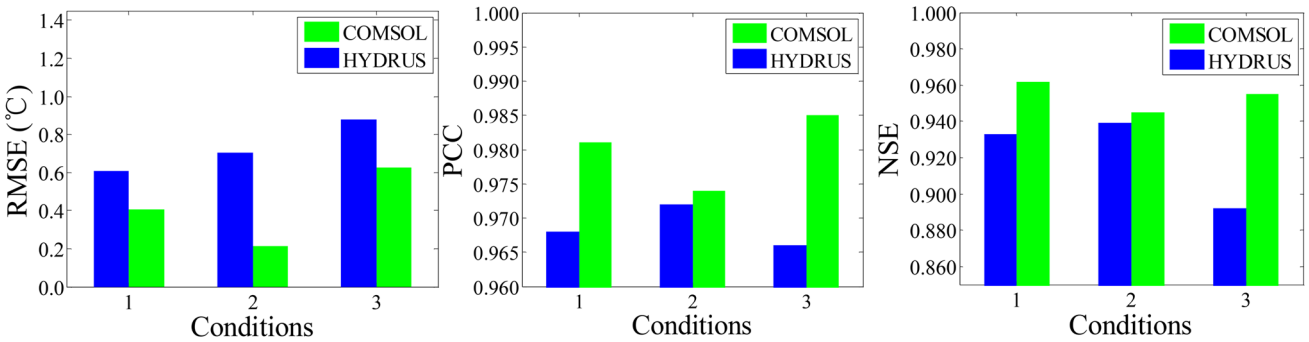

Fig. 7 Comparison of the root mean square error (RMSE), Pearson correlation coefficient (PCC) and Nash–Sutcliffe efficiency coefficient (NSE) of COMSOL and HYDRUS under different conditions in the domain

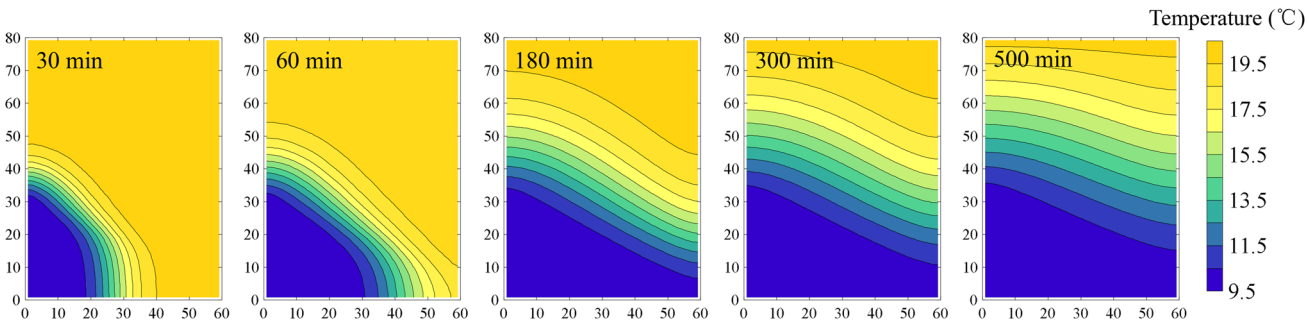

Fig. 8 The simulation results of temperature varied over time under Condition 1

Table 8 Factor levels of the orthogonal experiment

Level	H (cm)	T (°C)	k_s (m/s)	α (1/m)	n_v	θ_r (m^3/m^3)	θ_s (m^3/m^3)
1	27	8.55	7.425×10^{-5}	0.9	1.089	0.0207	0.3078
2	30	9.50	8.250×10^{-5}	1.0	1.210	0.0230	0.3420
3	33	10.45	9.075×10^{-5}	1.1	1.331	0.0253	0.3762

Table 9 Calculation schemes and results of the orthogonal experiment

Scheme	1	2 (H)	3 (T)	4 (k_s)	5 (α)	6 (n_v)	7 (θ_r)	8 (θ_s)	T (°C)
1	1	27	8.55	7.425×10^{-5}	0.9	1.089	0.0207	0.3078	14.624
2	1	27	9.50	8.250×10^{-5}	1.0	1.210	0.0230	0.3420	13.946
3	1	27	10.45	9.075×10^{-5}	1.1	1.331	0.0253	0.3762	13.741
4	1	30	8.55	7.425×10^{-5}	1.0	1.210	0.0253	0.3762	13.108
5	1	30	9.50	8.250×10^{-5}	1.1	1.331	0.0207	0.3078	12.829
6	1	30	10.45	9.075×10^{-5}	0.9	1.089	0.0230	0.3420	14.969
7	1	33	8.55	8.250×10^{-5}	0.9	1.331	0.0230	0.3762	11.608
8	1	33	9.50	9.075×10^{-5}	1.0	1.089	0.0253	0.3078	14.181
9	1	33	10.45	7.425×10^{-5}	1.1	1.210	0.0207	0.3420	13.959
10	2	27	8.55	9.075×10^{-5}	1.1	1.210	0.0230	0.3078	13.326
11	2	27	9.50	7.425×10^{-5}	0.9	1.331	0.0253	0.3420	13.168
12	2	27	10.45	8.250×10^{-5}	1.0	1.089	0.0207	0.3762	15.444
13	2	30	8.55	8.250×10^{-5}	1.1	1.089	0.0253	0.3420	14.150
14	2	30	9.50	9.075×10^{-5}	0.9	1.210	0.0207	0.3762	13.314
15	2	30	10.45	7.425×10^{-5}	1.0	1.331	0.0230	0.3078	13.515
16	2	33	8.55	9.075×10^{-5}	1.0	1.331	0.0207	0.3420	11.576
17	2	33	9.50	7.425×10^{-5}	1.1	1.089	0.0230	0.3762	14.375
18	2	33	10.45	8.250×10^{-5}	0.9	1.210	0.0253	0.3078	13.656

Table 10 The results of range sensitivity analysis for each factor's contribution to the index

	Factors	H	T	k_s	α	n_v	θ_r	θ_s
$\overline{T}$	K_1	0.4032	− 0.5729	0.1532	− 0.0818	0.9856	− 0.0139	0.0502
	K_2	0.0092	− 0.0028	− 0.0328	− 0.0099	− 0.0868	− 0.0151	− 0.0103
	K_3	− 0.4124	0.5757	− 0.1204	0.0917	− 0.8988	0.0291	− 0.0399
	R	0.8156	1.1486	0.2736	0.1735	1.8844	0.0442	0.0901
Sensitivity	n_v>T>H>k_s>α>θ_s>θ_r							

table of the sensitivity of the model parameters. The combination of factors corresponding to each row in the table was used as a test scheme. The orthogonal test calculation schemes and results are shown in Table 9.

According to the results of the orthogonal test shown in Table 9, range analysis was used to analyze the sensitivity of each parameter to the test index, and was applied to the mean temperature at 500 min. The results (Table 10) showed that the sensitivity of each factor to temperature ranged from large to small: n_v, T, H, k_s, α, θ_s, θ_r.

Within range analysis, the larger the range of a parameter, the greater the sensitivity, and the greater the impact on test indicators. Figure 9 shows that the parameters n_v, T and H

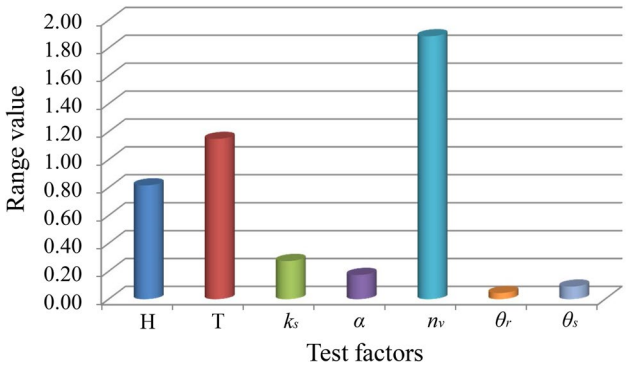

Fig. 9 Sensitivity contrast results of each test index

had considerable influence on temperature in the model, and the sensitivity of n_v was the greatest. The sensitivities of the parameters k_s, α, θ_r and θ_s were relatively small.

Conclusions

The current study used the Lu et al. (2007) model representing riparian zone saturated–unsaturated seepage and temperature. Simulation of soil hydro-thermal transmission and a laboratory test were used to validate the Lu et al. (2007) model against simulations of soil thermal conductivity by COMSOL Multiphysics. The distribution of temperature field in the riparian zone was also obtained. The present study made the following conclusions:

1. The analysis indicators (RMSE, PCC and NSE) of single observation points indicated that Lu et al. (2007) model and Horton thermal conductivity models each had their own advantages; therefore, it was difficult to determine which one was more suitable. Global analysis using the three experimental conditions found that the simulations of temperature of the riparian zone based on the Lu et al. (2007) model were in good agreement with the measured values.
2. The temperature of soil near the infiltration and bottom boundaries rapidly fell, reaching a steady state in a relatively short period of time, with temperature close to the infiltration water temperature. In contrast, more time was required for the temperature near the upper and right boundaries to reach a steady state. The influence of water temperature was more obvious closer to the infiltration boundary. With an increase in the infiltration head, average soil temperature decreased, the low-temperature region of the soil gradually expanded, and the temperature gradient increased.
3. The river channel and riparian zone conducted heat transfer through lateral hyporheic exchange, and obvious vertical temperature stratification occurred in the riparian aquifers, forming a non-isothermal soil environment under the bidirectional radiation of the low-temperature water layer and the upper natural temperature surface, and the gradient gradually decreased with depth. A temperature division into low, medium and high temperature zones was evident in the horizontal direction from offshore to the far shore. The spatial distribution of temperature changed with time, illustrating the spread of cold water and the gradual decrease in the temperature gradient.
4. The sensitivity of the orthogonal experiment was analyzed. Seven factors were considered: three factors for each parameter level and three levels of factors, with a reference value and an increase and decrease of the reference value by 10%, respectively. The parameters n_v, T and H were shown to have considerable influence on the temperature field in the model, and the sensitivity of n_v was the highest. The sensitivities of the parameters k_s, α, θ_r and θ_s were relatively small.

Acknowledgements This study was funded by CRSRI Open Research Program (Grant No. CKWV2017500/KY), and National Natural Science Foundation of China (Grant No. 51679194).

Compliance with ethical standards

Conflict of interest No conflicts of the interest are declared.

References

Alekseevich AN (2017) Numerical modelling of tailings dam thermal-seepage regime considering phase transitions. Model Simul Eng 4:1–10

Arntzen EV, Geist DR, Dresel PE (2006) Effects of fluctuating river flow on groundwater/surface water mixing in the hyporheic zone of a regulated, large cobble bed river. River Res Appl 22(8):937–946

Boutt DF, Fleming BJ (2009) Implications of anthropogenic river stage fluctuations on mass transport in a valley fill aquifer. Water Resour Res 45(4):546–550

Brunetti G, Saito H, Saito T, Šimůnek J (2017) A computationally efficient pseudo-3D model for the numerical analysis of borehole heat exchangers. Appl Energy 208:1113–1127

Brunetti G, Porti M, Patrizia P (2018) Multi-level numerical and statistical analysis of the hygrothermal behavior of a non-vegetated green roof in a mediterranean climate. Appl Energy 221:204–219

Casado A, Hannah DM, Peiry JL, Ferreras AMC (2013) Influence of dam-induced hydrological regulation on summer water temperature: Sauce Grande River, Argentina. Ecohydrology 6(4):523–535

Chui TFM, Freyberg DL (2007) The use of COMSOL for integrated hydrological modeling. In: COMSOL conference, Boston, pp 217–23

Chung SO, Horton R (1987) Soil heat and water flow with a partial surface mulch. Water Resour Res 23(12):2175–2186

Curry RA, Gehrels J, Noakes DLG, Swainson R (1994) Effects of river flow fluctuations on groundwater discharge through brook trout, *Salvelinus fontinalis*, spawning and incubation habitats. Hydrobiologia 277(2):121–134

Fritz B, Arntzen EV (2007) Effect of rapidly changing river stage on uranium flux through the hyporheic zone. Groundwater 45(6):753–760

Gardner WR, Hillel D, Benyamini Y (1970) Post-irrigation movement of soil water: 1. Redistribution. Water Resour Res 6(3):851–861

Gerecht KE, Cardenas MB, Guswa AJ, Sawyer AH, Nowinski JD, Swanson TE (2011) Dynamics of hyporheic flow and heat transport across a bed-to-bank continuum in a large regulated river. Water Resour Res 47(47):104–121

Giraldo NM, Bayer P, Blum P, Cirpka O (2011) Propagation of seasonal temperature signals into an aquifer upon bank infiltration. Groundwater 49(4):491–502

Harleman DRF (1982) Hydrothermal analysis of lakes and reservoirs. J Hydraul Div 108(3):301–325

Healy RW, Ronan AD (1996) Documentation of computer program VS2DH for simulation of energy transport in variably saturated porous media; modification of the US geological survey's computer program VS2DT. U.S. Geological Survey. Water-Resource Investigation Report 96-4230

Ho IH, Dickson M (2017) Numerical modeling of heat production using geothermal energy for a snow-melting system. Geomech Energy Environ 10:42–51

Kipp KL (1987) A computer code for simulation of heat and solution transport in three-dimensional groundwater flow systems. USGS Water Resources Investigations Report, Denver, pp 86–4095

Laganière J, Paré D, Bergeron Y, Chen HYH (2012) The effect of boreal forest composition on soil respiration is mediated through variations in soil temperature and C quality. Soil Biol Biochem 53:18–27

Liu Z, Yu X (2011) Coupled thermo-hydro-mechanical model for porous materials under frost action: theory and implementation. Acta Geotech 6(2):51–65

Lu S, Ren TS, Gong YS, Horton R (2007) An improved model for predicting soil thermal conductivity from water content at room temperature. Soil Sci Soc Am J 71(1):8–14

Mark O, Tony DA, Andrew JD (2012) Projected soil temperature increase and seed dormancy response along an altitudinal gradient: implications for seed bank persistence under climate change. Plant Soil 353(1–2):289–303

Milly PCD (1987) Estimation of the Brooks Corey parameters from water retention data. Water Resour Res 23:1085–1089

Nowinski JD, Cardenas MB, Lightbody AF, Sawyer A (2012) Hydraulic and thermal response of groundwater–surface water exchange to flooding in an experimental aquifer. J Hydrol 472–473(23):184–192

Oosterbaan H, Janiszewski M, Uotinen L, Siren T, Rinne M (2016) Numerical thermal back-calculation of the Kerava Solar Village underground thermal energy storage. Procedia Eng 191:352–360

Ren J, Wang XP, Shen ZZ, Zhao J, Yang J, Ye M, Zhou YJ, Wang ZH (2018) Heat tracer test in a riparian zone: laboratory experiments and numerical modelling. J Hydrol 563:560–575

Saito H, Šimůnek J, Mohanty BP (2006) Numerical analysis of coupled water, vapor, and heat transport in the vadose zone. Vadose Zone J 5(2):784–800

Shao W, Bogaard T, Bakker M (2014) How to use comsol multiphysics for coupled dual-permeability hydrological and slope stability modeling. Procedia Earth Planet Sci 9:83–90

Šimůnek J, Sejna M, van Genuchten MT (1999) HYDRUS-2D simulating water flow, heat, and solute transport in two-dimensional variably saturated media. International Ground Water Modeling Center, Riverside

van Genuchten MT (1980) A closed-form equation for predicting the hydraulic conductivity of unsaturated soils. Soil Sci Soc Am J 44:892–898

Vogt T, Schirmer M, Cirpka O (2012) Investigating riparian groundwater flow close to a losing river using diurnal temperature oscillations at high vertical resolution. Hydrol Earth Syst Sci 16(2):473–487

Wang JD, Gong SH, Xu D, Juan S, Mu JX (2013) Numerical simulations and validation of water flow and heat transport in a subsurface drip irrigation system using HYDRUS-2D. Irrig Drain 62(1):97–106

Wu ZW, Song HZ (2015) Numerical simulation of embankment dam seepage monitoring with temperature based on thermal-hydro coupling model. Rock Soil Mech 36:584–590 **(in Chinese)**

Xu C, Dowd PA, Tian ZF (2015) A simplified coupled hydro-thermal model for enhanced geothermal systems. Appl Energy 140:135–145

Yosef TY, Song CR, Chang KT (2017) Hydro-thermal coupled analysis for health monitoring of embankment dams. Acta Geotech 4:1–9

Zhao Y, Zhai XF, Wang ZH, Li HJ, Jiang R, Hill RL, Si B, Hao F (2018) Simulation of soil water and heat flow in ridge cultivation with plastic film mulching system on the Chinese Loess Plateau. Agric Water Manag 202:99–112